Solar Energy Materials & Solar Cells 230 (2021) 111191

Contents lists available at ScienceDirect

Solar Energy Materials and Solar Cells

journal homepage: www.elsevier.com/locate/solmat

Heat-concentrating solar steam generation and salt extraction based on water-repellent germanium nanoparticles-coated oxidized copper foams

Yisu Xu [a], Zhifu Qi [b,c], Zhouyang Luo [a,b,c], Zhen Shen [b,c], Chenxi Li [b,c], Guo Chen [a], Wenyi Cai [a], Hua Bao [a], Chang-Ching Tu [a,*]

[a] University of Michigan-Shanghai Jiao Tong University Joint Institute, Shanghai Jiao Tong University, Shanghai, 200240, China
[b] Key Laboratory of Solar Energy Utilization & Energy Saving Technology of Zhejiang Province, Hangzhou, 311121, China
[c] Zhejiang Energy Group R&D Institute Co., Ltd., Hangzhou, 311121, China

ARTICLE INFO

Keywords:
Heat concentration
Solar steam generation
Salt extraction
Germanium nanoparticles
Copper foams

ABSTRACT

We demonstrate solar steam generation with high evaporation rates and extraction of dry salts from solutions by using water-repellent germanium nanoparticles (GeNPs)-coated oxidized copper foams (CFs) as light absorbers and heat concentrators. The CF surface was first oxidized into black CuO, then dip-coated with colloidal GeNPs for enhancing infrared absorption, and lastly treated with perfluoroalkyl silane to render hydrophobicity. The CF can absorb more than 95% of the AM1.5G solar irradiance spectrum, for heating up a water-permeated cellulose paper underneath to generate steam which is then evacuated through the CF's interconnected pores. Furthermore, due to the CF's high thermal conductivity, the heat generated in the peripheral region can be efficiently concentrated to the center where the water evaporates. With the light-absorbing CF area about 7 times larger than the water-evaporating cellulose paper and the convective heat loss mitigated by an acrylic cover, under one sun solar irradiance, the CF temperature can reach 70 °C, resulting in an evaporation rate as high as 3.2 kg m^{-2} h^{-1}. Moreover, when a NaCl solution is used for the heat-concentrating evaporation inside an enclosed system in which the water condensate is recycled, readily useful dry salts are formed and can be harvested from the hydrophobic CF surface, while the bulk solution is gradually desalinized.

1. Introduction

Water is vital for all living organisms to grow and reproduce. Particularly, the great majority of mammals including human beings can only survive on freshwater which however comprises just less than 3% of the earth's water. Owing to the climate change and population growth, the demand and stress for freshwater continue to rise [1]. Desalination which converts saline water or sewage into freshwater, although usually expensive, can practically resolve the water scarcity issue in many arid areas [2]. Solar distillation can be a cost-effective, environmental-friendly and scalable way to produce freshwater [3,4].

Just similar to how the natural water cycle on earth is driven by the solar energy, a typical solar distillation process involves the evaporation of water which can be expedited by solar heating and the collection of water condensate inside the enclosed system. For conventional solar stills, the entire volume of water in the reservoir is heated up by absorbing sunlight, which inevitably leads to high heat loss [5]. In contrast, interfacial solar evaporation, in which the photothermal effect is localized at the evaporator surface and the whole evaporator is thermally insulated from the bulk water underneath, has shown a great potential to achieve high evaporation rates as well as high solar-to-vapor conversion efficiencies [6–8]. In general, efficient interfacial solar evaporators possess some key structural characteristics, including a light absorber which can convert a broad spectrum of solar radiation into heat, interconnected or perforated pores through which water is evaporated and transported by capillary force, and a floating base with low thermal conductivity for preventing conductive heat loss to the bulk water [9–22].

Depending on the photothermal conversion mechanism, various light-absorbing materials have been explored for the interfacial solar evaporation (Supporting Information (SI) Table S1). For example, plasmonic nanostructures combined with porous templates, such as Au nanoparticles deposited on an airlaid paper or alumina scaffold, Ag nanoparticles deposited on diatomite and Al nanoparticles self-assembled into a three-dimensional porous membrane [9–12], have shown remarkable photothermal conversion efficiencies owing to the

* Corresponding author.
E-mail address: changching.tu@sjtu.edu.cn (C.-C. Tu).

https://doi.org/10.1016/j.solmat.2021.111191
Received 3 February 2021; Received in revised form 29 April 2021; Accepted 15 May 2021
Available online 29 May 2021

localized surface plasmon resonance. However, the relatively high material cost hinders their widespread applications. On the other hand, carbon-based materials, such as carbon black powder, exfoliated graphite, functionalized graphene, carbon-based biomass and carbon nanotube composites [13–17], and polymer-based materials, such as polymer porous foams, hydrogel composites and ionic polymer nanowires [18–20], have demonstrated broad absorption of the solar spectrum while being low-cost and durable. In addition, a wide variety of inorganic nanomaterials with unique optical and structural properties, such as $Cu_{2-x}S$ nanowires, Ti_2O_3 nanoparticles, black titania nanocages, MoO_{3-x} quantum dots and Fe_3O_4 microspheres [21–25], have also shown their distinctive merits for the interfacial solar evaporation.

While being clean and inexhaustible, one major issue of solar energy is its relatively low energy density compared to other energy sources. As a result, in the process of solar steam generation, optical concentration systems are often employed to enhance the solar flux [26], so that the evaporation rate can be increased and more steam can be generated in a relatively short time. Typical optical concentration systems may include parabolic trough collectors, heliostat field collectors, linear Fresnel reflectors and parabolic dish collectors [27]. Although the solar flux can be concentrated tens or even thousands times, the optical concentrating systems are usually quite expensive [28]. Recently, a much more cost-effective heat concentration approach was demonstrated. With the suppressed radiative, convective and conductive losses, the solar generated heat can be efficiently concentrated by a copper film to an evaporation slot where 100 °C steam was generated under ambient air condition without optical concentration [29].

In the first part this work, we demonstrate heat-concentrating interfacial solar steam generation with high evaporation rates by using water-repellent germanium nanoparticles (GeNPs)-coated oxidized copper foams (CFs) as light absorbers and heat concentrators (Fig. 1A). The CF can absorb more than 95% of the AM1.5G solar irradiance spectrum to generate heat which is then transferred to a water-permeated cellulose paper underneath. Both the water-repellent CF and the water-permeated cellulose paper are thermally insulated from the bulk water by expanded polystyrene foam. As the water absorbs the heat and evaporates, the CF's interconnected pores can facilitate steam evacuation, while the two ends of the cellulose paper are submerged in the bulk water for continuously sucking and transporting water through capillary force. Furthermore, owing to the CF's high thermal conductivity and hydrophobic surface property, when the light absorption area (i.e. the CF size) larger than the water evaporation area (i.e. the cellulose paper size), the heat generated in the peripheral region can be efficiently concentrated to the center where the water evaporates. As a result, the CF temperature and thus the evaporation rate can be greatly enhanced.

The major byproduct from coastal seawater desalination is the highly concentrated solution of salts which, if directly discharged into the sea, may exert adverse effects on the marine ecosystem [30], and many precious minerals and metals contained in the seawater, such as chloride, sodium, magnesium and sulphur, will be wasted. Traditionally, electrodialysis is used to extract salts from the brine [31], which however has high energy demands and requires the pre-treatment of feedwater. As a green alternative to the electrodialysis method, in the second part of this work, we demonstrate the extraction of dry salts from NaCl solutions by using a similar setup as shown in Fig. 1A, except that the heat-concentrating solar steam generation occurs in an enclosed system in which the water condensate is recycled (Fig. 1B). As the water evaporates rapidly from the cellulose paper, the highly concentrated solutes accumulating on the cellulose paper cannot diffuse back to the bulk solution in time. As a result, dry salts start to grow and remain on the hydrophobic CF surface. As the solar irradiation continues, more and more readily useful dry salts can be harvested, while the bulk solution is gradually desalinized.

2. Experimental results

2.1. Synthesis and characterization of the GeNPs

The synthesis of the GeNPs was based on a high-energy ball milling method developed previously with some modifications (SI Fig. S1) [32]. Firstly, a crystalline Ge wafer was pulverized into GeNPs by prolonged high-energy ball milling with zirconia beads in isopropanol. Then, the GeNPs were treated with diluted HF for removing surface oxidation and creating Ge–H terminations, followed by a heat induced hydrosilylation reaction with neat 10-Undecen-1-ol (10-UD-ol) in an oxygen free environment. After purification, the 10-UD-ol passivated GeNPs formed uniform and stable suspension in tetrahydrofuran (THF) for the following experiments. As shown in the transmission electron microscope (TEM) images (Fig. 2A) and the dynamic light scattering (DLS) particle size distribution (Fig. 2B), the GeNPs have irregular flaky shapes with the majority particle size ranging from about 100 nm to 400 nm. In addition, the X-ray powder diffraction (XRD) analysis (Fig. 2C) shows that the GeNPs are polycrystalline, despite the fact that the Ge wafer as the source material is single crystalline (SI Fig. S2). Such crystallinity transformation may be due to the change of surface strain caused by the high-energy ball milling process. Similar phenomena were also found for the Ti_2O_3 and Si nanoparticles [22,32].

The surface chemistry of the GeNPs, as shown in the Fourier-transform infrared (FTIR) microscopy spectrum (Fig. 2D), is characterized by a primary absorption peak associated with the Ge–O−Ge stretching (746 cm^{-1}), which is analogous to the Si–O–Si stretching (1100 cm^{-1}) found for both Si nanoparticles and Si quantum dots [32, 33]. Other absorption peaks due to the Ge–C rocking (848 cm^{-1}), CH_2 bending (1450 cm^{-1}) and CH_2 stretching (2860 and 2930 cm^{-1}) confirm the passivation of the 10-UD-ol ligands on the GeNP surfaces. Based on the absorbance spectra of the GeNP suspensions with different concentrations (SI Fig. S3), the molar extinction coefficient spectrum (red curve in Fig. 2E) is obtained. The colloidal GeNPs in THF have high molar

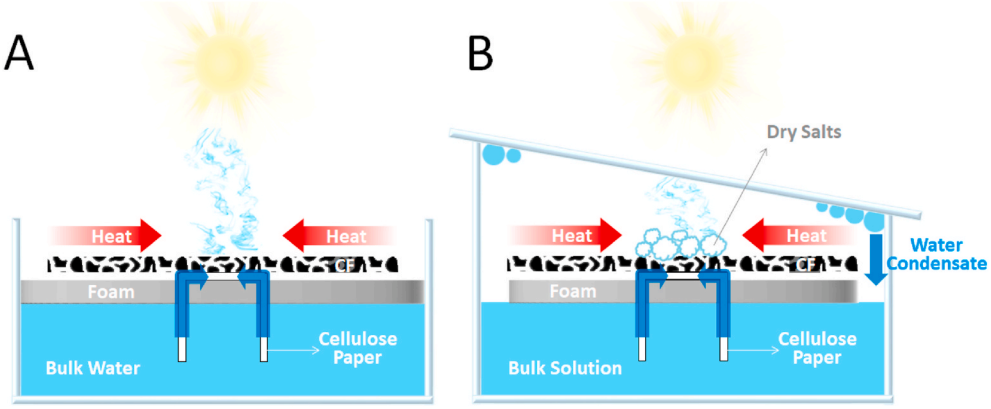

Fig. 1. (A) Schematic cross-section of the heat-concentrating interfacial solar steam generation setup, including a water-repellent GeNPs-coated oxidized CF as the light-absorber and heat-concentrator, a water-permeated cellulose paper underneath the CF and a layer of expanded polystyrene foam which thermally insulate the water-repellent CF and the water-permeated cellulose paper from the bulk water. (B) Schematic cross-section of the heat-concentrating salt extraction setup which is similar to (A), except that the container is covered with a glass slide which is slightly tilted by about 10° for facilitating the water condensate to go back to the bulk solution.

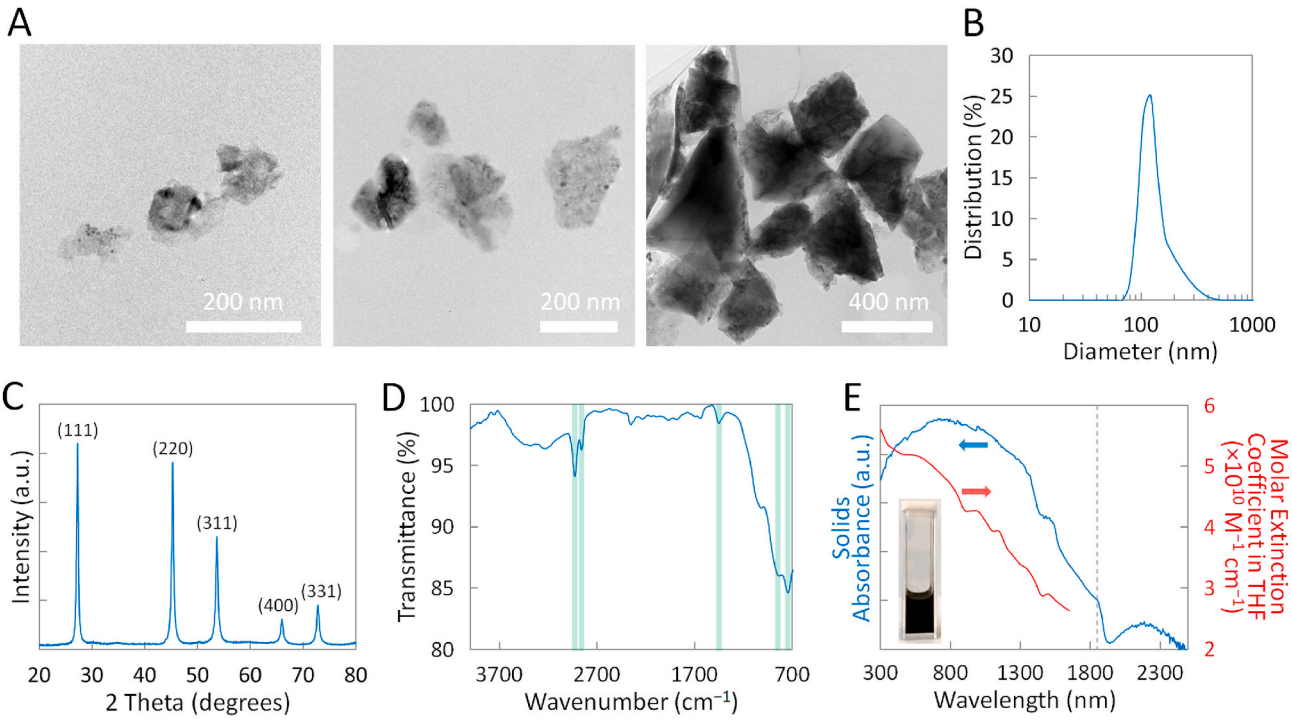

Fig. 2. (A) TEM images of the GeNPs in different size ranges. (B) DLS particle size distribution of the GeNPs dispersed in THF. (C) XRD pattern of the GeNP powder, manifesting its polycrystalline property. (D) FTIR microscopy spectrum of the GeNP powder. The green highlighted wavenumbers from left to right correspond to the CH_2 asymmetric stretching (2930 cm^{-1}), CH_2 symmetric stretching (2860 cm^{-1}), CH_2 bending (1450 cm^{-1}), Ge–C rocking (848 cm^{-1}) and Ge–O−Ge symmetric stretching (746 cm^{-1}). (E) Molar extinction coefficient spectrum of the GeNP suspension in THF (red curve) and absorbance spectrum of the dry GeNP powder mixed with $BaSO_4$ (blue curve). The inset shows the GeNP suspension in THF under room light. (For interpretation of the references to color in this figure legend, the reader is referred to the Web version of this article.)

extinction coefficients of more than 5×10^{10} M^{-1} cm^{-1} in the visible range and more than 2×10^{10} M^{-1} cm^{-1} in the near infrared (NIR) range. In comparison, 34-nm diameter citrate capped plasmonic gold nanoparticles in water have a molar extinction coefficient equal to 6.1×10^9 M^{-1} cm^{-1} at the surface plasmon resonance wavelength (506 nm) [34]. On the other hand, the absorbance spectrum of the dry GeNP powder mixed with $BaSO_4$ (blue curve in Fig. 2E), which resembles how the GeNPs are coated on the CF surface in this work, exhibits a similar trend as the molar extinction coefficient spectrum. Particularly, a minor absorption peak located at wavelengths longer than the Ge band gap energy (0.67 eV, 1.85 μm) is observed, which can be attributed to the surface and/or dangling defect states lying within the energy band gap [35].

2.2. Fabrication and characterization of the water-repellent GeNPs-Coated oxidized CFs

In this work, we use three types of CFs, each having different pores-per-inch (PPI) values and thicknesses, including 95-PPI (average pore size = 267 μm) with 5 mm in thickness, 130-PPI (average pore size = 195 μm) with 2 mm in thickness and 500-PPI (average pore size = 51 μm) with 1 mm in thickness. Besides, the 267-μm, 195-μm and 51-μm pore size CFs have densities equal to 0.415, 0.320 and 3.276 g cm^{-3}, corresponding to porosities of 95%, 96% and 63%, respectively. The fabrication process of the water-repellent GeNPs-coated oxidized CF is briefly described as follows. The CF was first cleaned by bath sonication in acetone, isopropanol and 1 M HCl sequentially, followed by oxidation in 2.5 M NaOH and 0.1 M $K_2S_2O_8$ to form black CuO on the CF surface. Then, the oxidized CF was submerged in the GeNP suspension (8 mg mL^{-1} in THF) and subsequently withdrawn for the dip-coating of the 10-UD-ol passivated GeNPs. Lastly, the GeNPs-coated oxidized CF was treated with Trichloro (1H,1H,2H,2H-perfluorooctyl)silane (TCPFOS) to render surface hydrophobicity. It is worth noting that the TCPFOS can be grafted on the CuO surface, as well as the coated GeNPs through coupling between the trichlorosilane and the hydroxyl termination of the 10-UD-ol ligand.

From the scanning electron microscope (SEM) images and the energy dispersive X-ray (EDX) analysis, the clean CFs have high copper purity and smooth microscopic surfaces, except the 51-μm pore size CF which shows relatively obvious granular structures (Fig. 3A–C and L). After the $NaOH/K_2S_2O_8$ oxidation, the oxygen concentration increases (Fig. 3M) and the CF surface becomes highly porous with submicron-scale, densely-packed, petal-like structures covering all over the macroscopic framework (Fig. 3D–F and J). The Raman spectrum and XRD pattern of the oxidized CF (SI Fig. S4) further confirms that the porous surface structure here is composed of CuO. Lastly, after the dip-coating of GeNPs and treatment of TCPFOS, the fluorine, germanium and carbon concentrations arise (Fig. 3N), whereas the surface roughness slightly decreases (Fig. 3G–I). Particularly, at high magnification, the GeNP clusters deposited on top of the CuO porous surface are clearly visible (Fig. 3K). Compared to the oxidized CF, the CF after the dip-coating of GeNPs and treatment of TCPFOS shows additional FTIR absorption peaks due to the CH_2 stretching (2860 and 2930 cm^{-1}) and the CF_2 stretching (1150 and 1200 cm^{-1}), which belong to the hydrocarbon chain of 10-UD-ol and the perfluoroalkyl chain of TCPFOS, respectively (SI Fig. S5). Furthermore, grafted with the TCPFOS's perfluoroalkyl chains, the CF surface becomes highly hydrophobic, with the contact angles as high as 130°, 117° and 116° for the 267-μm, 195-μm and 51-μm pore size CFs, respectively (SI Fig. S6). As a result, a water droplet can hardly wet the water-repellent GeNPs-coated oxidized CF surface (SI Video S1A). In contrast, a water droplet is quickly absorbed into the $NaOH/K_2S_2O_8$ oxidized CF (SI Video S1B).

The absorption spectra of the CFs with different structural properties and surface modifications are shown in Fig. 4, where absorption = 1 –

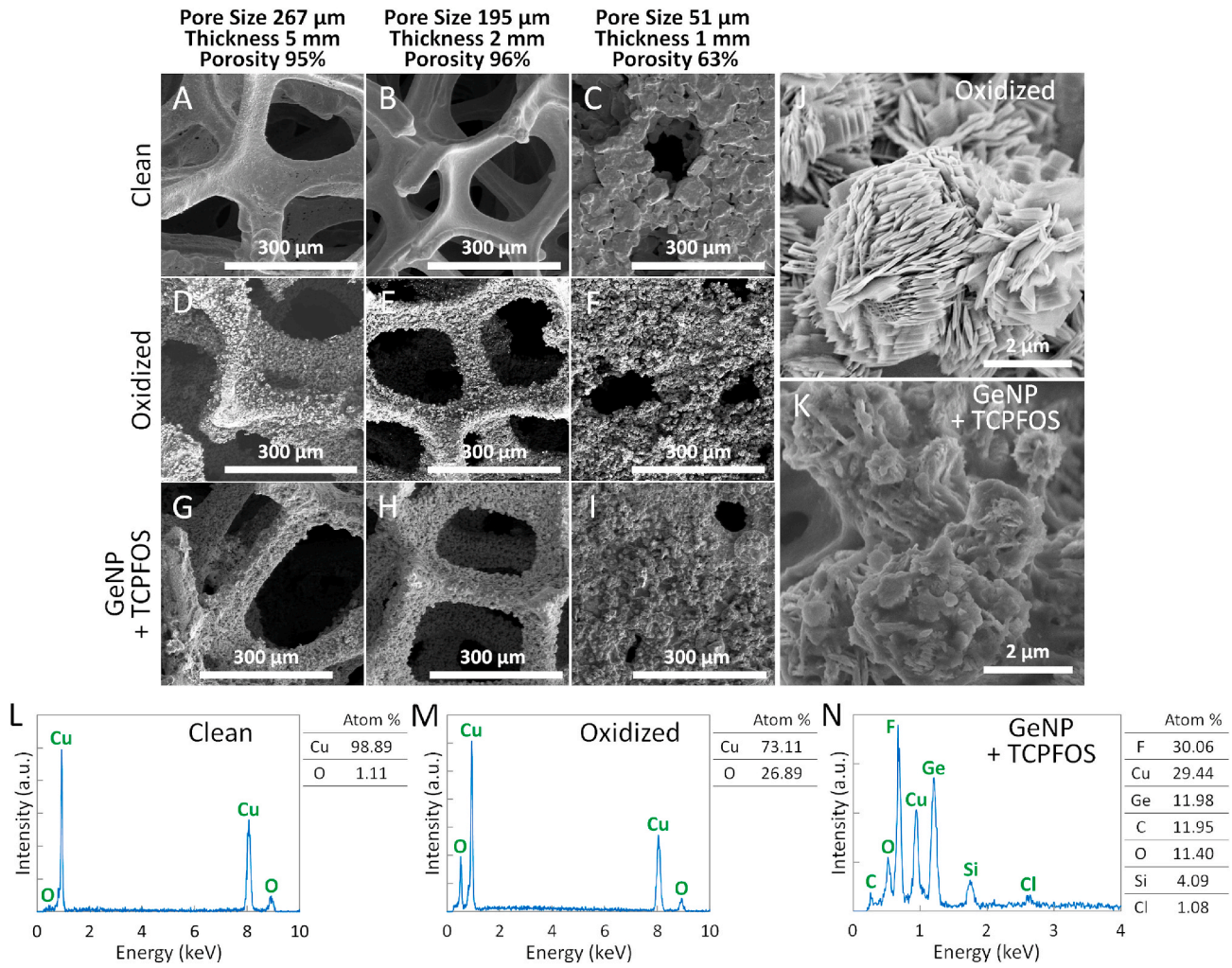

Fig. 3. (A–I) SEM images of the 267-µm, 195-µm and 51-µm pore size CFs in the clean condition, after the NaOH/$K_2S_2O_8$ oxidation, and after the dip-coating of GeNPs and treatment of TCPFOS, respectively. (J and K) High magnification SEM images of the oxidized and the water-repellent GeNPs-coated oxidized CFs, respectively. (L–N) EDX analysis results of the 267-µm pore size CFs in the clean condition, after the NaOH/$K_2S_2O_8$ oxidation, and after the dip-coating of GeNPs and treatment of TCPFOS, respectively.

transmission – reflection. The corresponding transmission and reflection spectra, which were measured by using an integrating sphere coupled to a UV–visible spectrophotometer, are shown in SI Fig. S7. The main absorption of the clean CFs lies below 600 nm (red curves in Fig. 4A–C), elucidating the CFs' yellowish brown color under room light (left photographs in Fig. 4D–F). After the NaOH/$K_2S_2O_8$ oxidation, due to the formation of porous CuO, all the oxidized CFs have more than 95% absorption from 200 nm to 800 nm and more than 85% absorption in the NIR range (green curves in Fig. 4A–C). The two regions are separated by a step-like transition which should stem from the steep downward slope observed in the clean condition absorption curve. Due to the nearly complete absorption in the visible range, the oxidized CFs look coal black under room light (middle photographs in Fig. 4D–F). Similar spectral characteristics have also been observed for other oxidized CFs in literature [36]. Lastly, after the dip-coating of GeNPs and treatment of TCPFOS, the absorption spectra in the visible range remain almost unchanged (blue curves in Fig. 4A–C), although the CF colors become slightly grayish under room light (right photographs in Fig. 4D–F). Meanwhile, the light-absorbing ability in the NIR range, particularly from 800 to 1500 nm, is further increased, with the 195-µm pore size CF showing the most significant improvement. Under solar irradiation, the water-repellent GeNPs-coated oxidized CFs, with all the pore sizes, thicknesses and porosities, can achieve more than 95% absorption of the AM1.5G solar irradiance spectrum (SI Fig. S8).

2.3. Heat-concentrating solar steam generation

Next we characterize the heat-concentrating solar steam generation of the water-repellent GeNPs-coated oxidized CFs (Fig. 5), by using the setup as shown in Fig. 1A. During the whole evaporation process, the liquid water, despite in direct contact with the CF, resides only within the cellulose paper, whereas the generated steam can evacuate through the CF's interconnect pores. Here the evaporation rates and the solar-to-vapor conversion efficiencies are calculated with the dark evaporation subtracted. When the light-absorbing CF and the water-evaporating cellulose paper have the same size, 2 cm × 2 cm, under one sun solar irradiance, the evaporation rates and the conversion efficiencies of the 267-µm, 195-µm and 51-µm pore size CFs are equal to 0.97, 1.09 and 0.98 kg m^{-2} h^{-1} and 65%, 72% and 65%, respectively (Fig. 5A–C and i in Fig. 5J–L). While all three CFs have similar temperatures around 46 °C, the 195-µm pore size CF exhibits a little higher evaporation rate, because of the relatively large pore size and the relatively small thickness, both of which can facilitate steam evacuation. In comparison, a "hydrophilic" CF having the same area and pore size, but only oxidized by the NaOH/$K_2S_2O_8$ without the following surface treatment steps, shows a higher evaporation rate and a higher conversion efficiency of 1.35 kg m^{-2} h^{-1} and 89% but a lower CF temperature of 39 °C (SI Fig. S9). This result demonstrates that although the CF's hydrophobic surface property enables the heat concentration and salt extraction, the

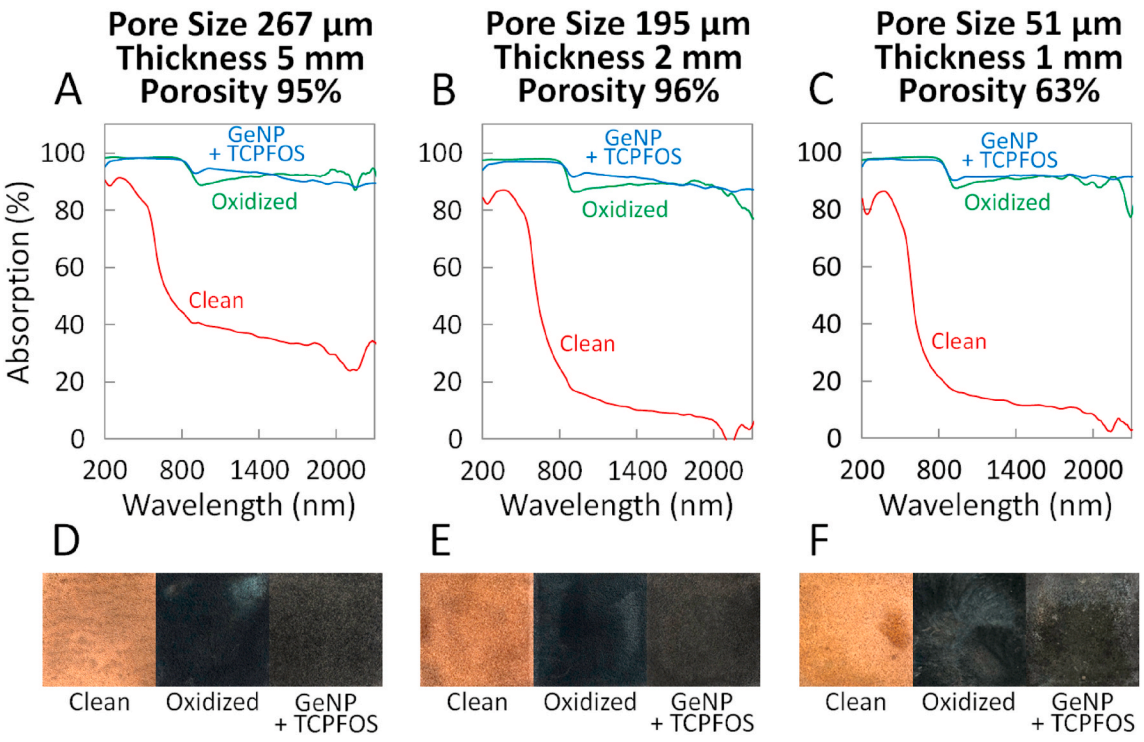

Fig. 4. (A–C) Absorption spectra and (D–F) photographs of the 267-μm, 195-μm and 51-μm pore size CFs in the clean condition, after the NaOH/$K_2S_2O_8$ oxidation, and after the dip-coating of GeNPs and treatment of TCPFOS, respectively.

heat transfer from the hydrophilic CF to the water is more efficient than the heat transfer from the hydrophobic CF to the water.

When the CF is enlarged to a 6 cm diameter disk with the underlying cellulose paper size kept unchanged, the heat generated around the peripheral region of the CF can be efficiently concentrated to the center. As a result, the central CF temperatures rise to more than 60 °C, leading to high evaporation rates equal to 2.78, 2.30 and 2.79 kg m^{-2} h^{-1} for the 267-μm, 195-μm and 51-μm pore size CFs, respectively (Fig. 5D–F and ii in Fig. 5J–L). Compared to the condition without heat concentration (Fig. 5A–C), here the evaporation rates are about two to three times larger. However, the higher CF temperature also leads to the more heat loss, especially through convection (bout 30%) and radiation (about 35%) (SI Fig. S10). As a result, the conversion efficiencies drop to the range between 20% and 30%. It is worth noticing that in comparison with the other two CFs, the 51-μm pore size CF with the much higher thermal conductivity (65.3 W m^{-1} K^{-1}) shows the strongest heat-concentrating ability, as indicated by the merely 1 °C temperature difference between the central and peripheral regions. In contrast, the 195-μm pore size CF, due to its relatively low thermal conductivity (8.1 W m^{-1} K^{-1}) and small thickness which leads to small cross-section, cannot transfer the heat as efficiently, resulting in about 10 °C temperature difference between the central and peripheral regions.

To mitigate the convective heat loss, a 1-mm thick poly (methyl methacrylate) (PMMA) slab with a 2 cm × 2 cm hole at the center is placed on top of the CF. In addition, a 5-mm air gap is kept in between the two parts and the hole position is well aligned with the cellulose paper. After adding the PMMA cover, the central CF temperatures and the evaporation rates further increase to 69.3 °C, 64.8 °C and 74.3 °C and 2.96, 2.63 and 3.19 kg m^{-2} h^{-1} for the 267-μm, 195-μm and 51-μm pore size CFs, respectively. At the same time, the conversion efficiencies also improve to almost 30% (Fig. 5G–I and iii in Fig. 5J–L). Compared to other heat-concentrating solar evaporators for which the conversion efficiency is about 30% at the vapor temperature about 80 °C [26], here the 51-μm pore size CF with the PMMA cover achieves comparable performance with the conversion efficiency equal to 29.1% and the central CF temperature, which should be close to the vapor temperature, equal to 74.3 °C. Note that if there is no cellulose paper, the 195-μm pore size CF alone under one sun solar irradiance can reach temperatures as high as 70.1 °C and 80.5 °C, with and without the PMMA cover, respectively (SI Fig. S11). In contrast, having the 2 cm × 2 cm water-evaporating cellulose paper underneath, the central CF temperatures with and without the PMMA cover were equal to 60.0 °C and 64.8 °C, respectively (Fig. 5E and H).

It is worth noticing that if the PMMA cover is placed directly on top of the CF surface without air gap, water condensate adhering to the PMMA cover inner surface would appear during the steam generation process, particularly for the 267-μm pore size CF. This observation demonstrates that the steam can not only evacuate vertically, but also propagate horizontally through the CF's interconnected pores and then escape from the CF's peripheral region. Therefore, it is critical to keep an appropriate air gap, so that there is sufficient lateral air flow to take away the steam trapped between the PMMA cover and the CF, while the vertical convective heat loss over the CF's peripheral region is mitigated. Other approaches to prevent heat loss, such as increasing the thickness of the expanded polystyrene foam, would yield relatively limited improvement of the conversion efficiency, given that the conduction heat loss constitutes only a small portion (about 5%) of the total heat loss (SI Fig. S10).

2.4. Heat-concentrating salt extraction

Next we first characterize the relationship between the heat-concentrating water evaporation and salt accumulation (Fig. 6), and then demonstrate salt extraction by taking advantage of the phenomenon observed (Fig. 7). Here 3.5 wt% NaCl aqueous solutions were used for the experiments. In general, as the water evaporates, the salts, although temporarily accumulating on the evaporator surface, will eventually diffuse back to the bulk solution to achieve salt rejection [36–38]. However, in this work, the water evaporation rate is greatly enhanced due to the heat concentration, such that the "wet salts" (i.e. the highly concentrated solutes) accumulating on the cellulose paper cannot diffuse back to the bulk solution in time. As a result, the salts

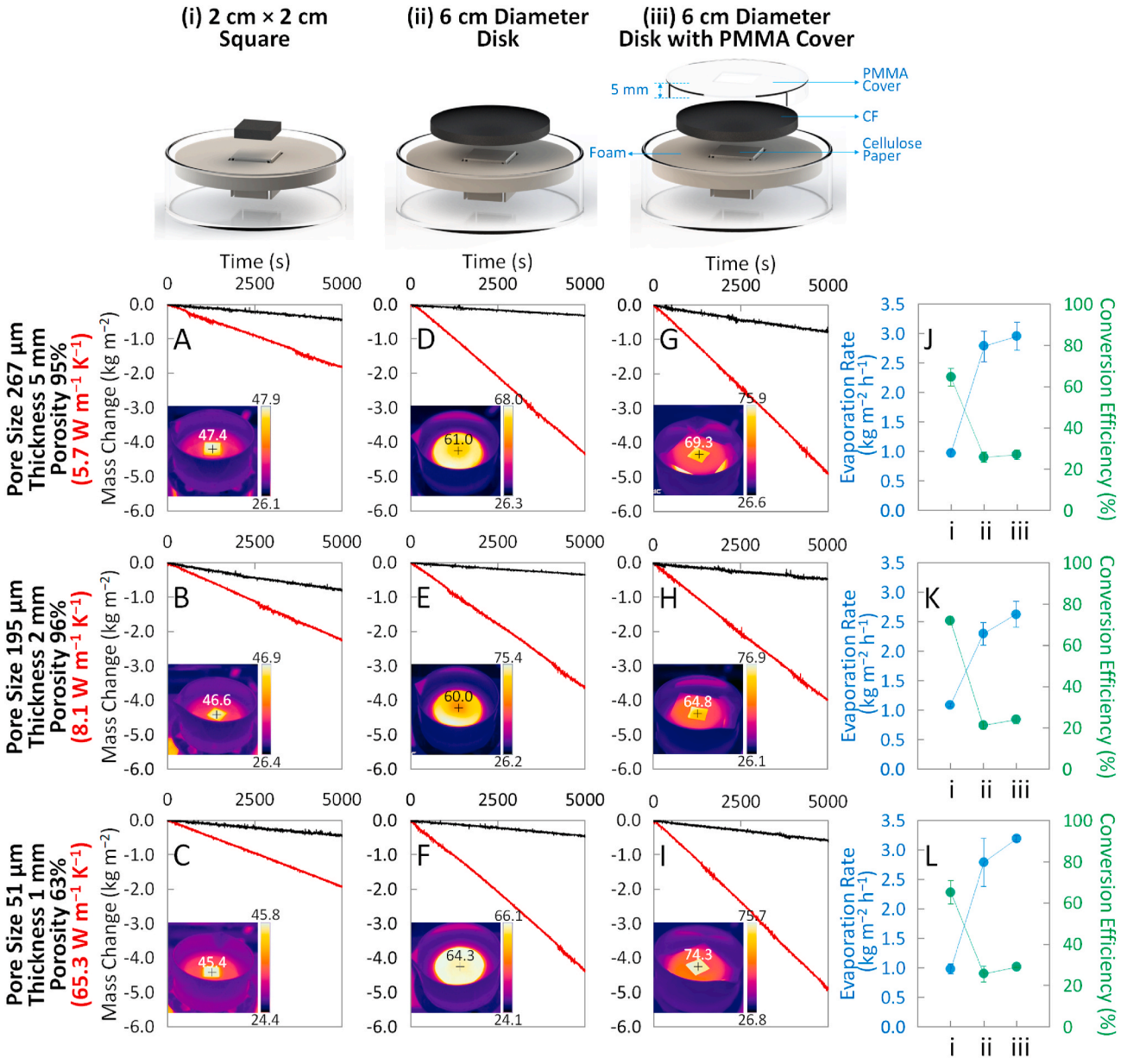

Fig. 5. Water evaporation mass change over time obtained in dark (black curves) and under one sun solar irradiance (red curves) for the 267-μm, 195-μm and 51-μm pore size, water-repellent GeNPs-coated oxidized CFs in different geometries, including (A–C) 2 cm × 2 cm square, (D–F) 6 cm diameter disk and (G–I) 6 cm diameter disk, while having the PMMA cover atop. Here the underlying cellulose paper size is constantly 2 cm × 2 cm. The insets are infrared images of the solar steam generation setups including the CFs at the center. The 267-μm, 195-μm and 51-μm pore size CFs have the thermal conductivities equal to 5.7, 8.1 and 65.3 W m^{-1} K^{-1}, respectively. (J–L) Evaporation rates (blue curves) and solar-to-vapor conversion efficiencies (green curves) calculated based on the mass change curves in (A–I), for the 267-μm, 195-μm and 51-μm pore size, water-repellent GeNPs-coated oxidized CFs in different geometries. Here the conversion efficiency (η) is calculated by $\eta = \frac{RA_{paper}h_{LV}}{A_{CF}q_{solar}}$, where R is the water evaporation rate with the dark evaporation subtracted (kg m^{-2} s^{-1}), A_{paper} is the cellulose paper area (m^2), h_{LV} is the heat of vaporization (2406–2333 kJ kg^{-1} at 40 °C–70 °C), A_{CF} is the CF area (m^2) and q_{solar} is the one sun solar irradiance (1 kW m^{-2}). Here deionized water was used for the experiments. (For interpretation of the references to color in this figure legend, the reader is referred to the Web version of this article.)

gradually pile up, infiltrating through the CF's pores, and finally become "dry salts" on the CF surface. Experimentally, with the cellulose paper size decreased from 4 cm × 4 cm–1 cm × 1 cm and the CF size kept constant at 6 cm in diameter, the average water evaporation rate increases from 1.49 to 7.92 kg m^{-2} h^{-1}. Accordingly, the dry salt accumulation rate increases from 0.026 to 0.208 kg m^{-2} h^{-1} (Fig. 6A and B). Moreover, the ratio of the dry salt accumulation rate to the average water evaporation rate also increases from 1.72 wt% to 2.63 wt% as the cellulose paper size decreased from 4 cm × 4 cm–1 cm × 1 cm (inset in Fig. 6B). Given that the initial NaCl concentration of the bulk solution is 3.5 wt%, the theoretical maximum of the ratio is 3.5/(100–3.5) = 3.63 wt% if there is no salt diffusion from the cellulose paper to the bulk solution during the evaporation process.

Unlike conventional interfacial solar evaporators whose evaporation rates decrease if there is light blocking or water channel clogging salt fouling on the surface, here the dry salts do not deteriorate the solar steam generation because of the following reasons: (1) The dry salts only appear on the CF surface as the whole CF remains completely dry during the evaporation process due to its hydrophobic surface property (SI Fig. S6 and SI Video S1A). In contrast, the wet salts, which can diffuse back to the bulk solution, exist on the cellulose paper. (2) The dry salts are usually formed at the central part of the CF, leaving the other parts

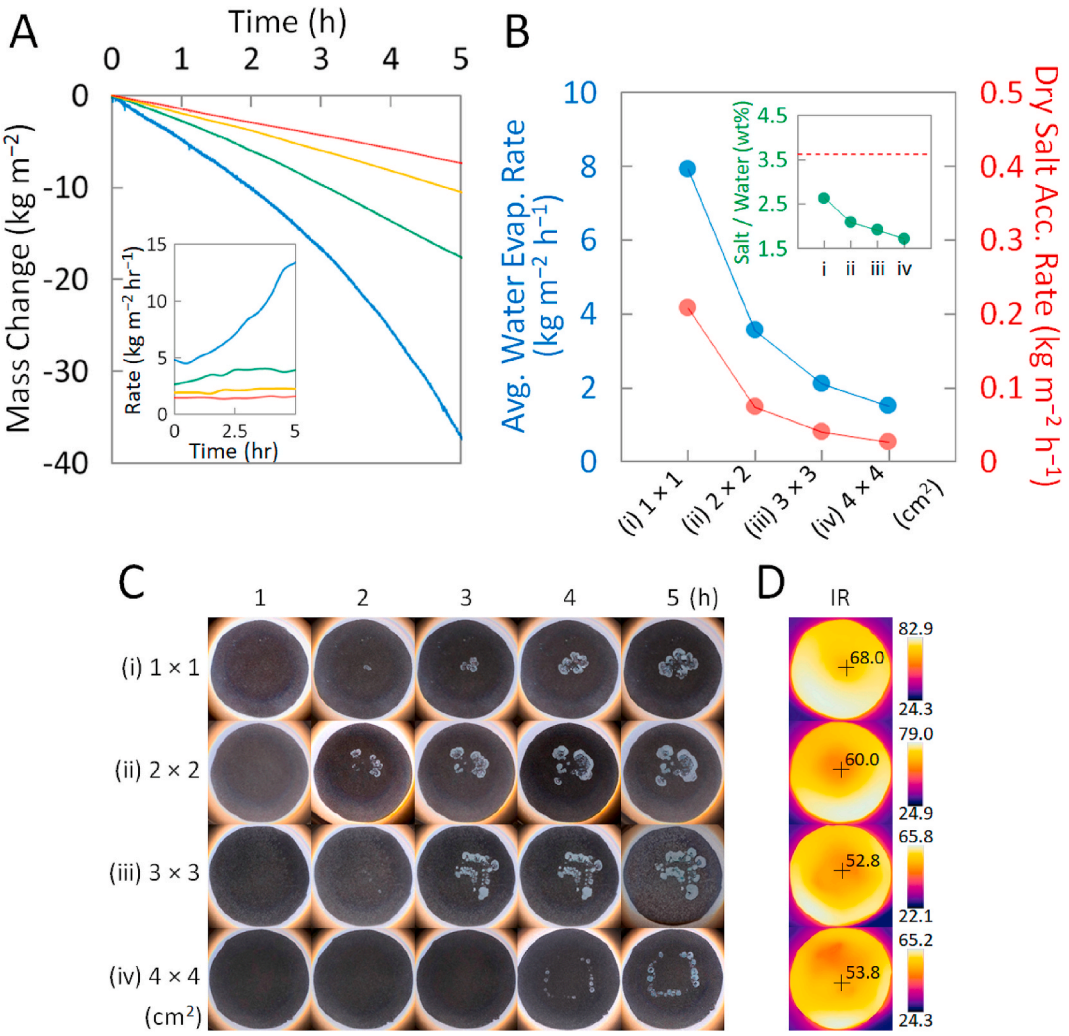

Fig. 6. (A) Water evaporation mass change over time for the 195-μm pore size, water-repellent GeNPs-coated oxidized CFs in 6 cm diameter disk with different underlying cellulose paper sizes, including 1 cm × 1 cm (blue curve), 2 cm × 2 cm (green curve), 3 cm × 3 cm (orange curve) and 4 cm × 4 cm (red curve). The inset shows the time-resolved water evaporation rates obtained from the corresponding mass change curves. The evaporation rate gradually increases for the CFs with the 1 cm × 1 cm and 2 cm × 2 cm cellulose paper sizes (blue and green curves), while the CFs with other cellulose paper sizes exhibit relatively stable evaporation rates. (B) Average water evaporation rates (blue curve) and dry salt accumulation rates (red curve) over 5 h for the CFs in (A). The inset shows the ratio between the red curve and the blue curve. As the cellulose paper size decreases, the ratio increases. The theoretical maximum of the ratio (red dash line) is 3.63 wt%. (C) Photographs of the CFs in (A) taken at each hour during the evaporation process. (D) Infrared images of the CFs in (A) taken at the second hour of the evaporation process. (For interpretation of the references to color in this figure legend, the reader is referred to the Web version of this article.)

intact for light absorption, and the generated heat can be efficiently concentrated to the evaporation sites owing to the CF's high thermal conductivity (Fig. 5E). (3) Although the dry salts may block the steam evacuation passage above the cellulose paper, the steam can still propagate horizontally through the CF's interconnected pores and escape from elsewhere.

Experimentally, the evaporation rates remain relatively stable or even increase when the dry salts are growing on the CF surface (inset in Fig. 6A). At relatively high accumulation rates, the rapidly accumulating wet salts may extend laterally on the expanded polystyrene foam surface while stacking upward, resulting in an effective evaporation area larger than the cellulose paper size. Therefore, for the CFs with small cellulose paper sizes, especially 1 cm × 1 cm, the evaporation rates gradually increase during the evaporation process (blue curve in Fig. 6A). If the cellulose paper size kept the same but the NaCl concentration increased, the same phenomenon of increasing evaporation rate was also observed (SI Fig. S12). In addition, the formation of dry salts usually begins at the cellulose paper edges where the evaporation rate, which is proportional to the CF temperature, is relatively high (Fig. 6C and D). This phenomenon is most prominent for the CF with the underlying cellulose paper size equal to 4 cm × 4 cm, on which the dry salts are well aligned with the cellulose paper perimeter. Lastly, with the 1 cm × 1 cm and 2 cm × 2 cm cellulose paper sizes, the formation of dry salts began at the second hour of the evaporation process. In contrast, no dry salt was observed until the forth hour with the 4 cm × 4 cm cellulose paper size. This observation is consistent with the cellulose paper size-dependent dry salt accumulation rates (red curve in Fig. 6B).

Furthermore, the long-term stability of the CFs as heat-concentrating solar evaporators was investigated (SI Fig. S13). When the deionized water was used for the study, no decay of the evaporation rate was observed after ten full evaporation cycles, each cycle comprising 3 h of one sun illumination, followed by 21 h of rest in dark. On the other hand, when the 3.5 wt% NaCl solution was used, the evaporation rate gradually increased as the fast accumulating wet salts expanded beyond the cellulose paper area, which was also the cause of the increasing evaporation rate of the 1 cm × 1 cm CF described previously (blue curve in Fig. 6A). With either deionized water or 3.5 wt% NaCl, the font surfaces of the CFs maintained completely dry throughout the whole long-term

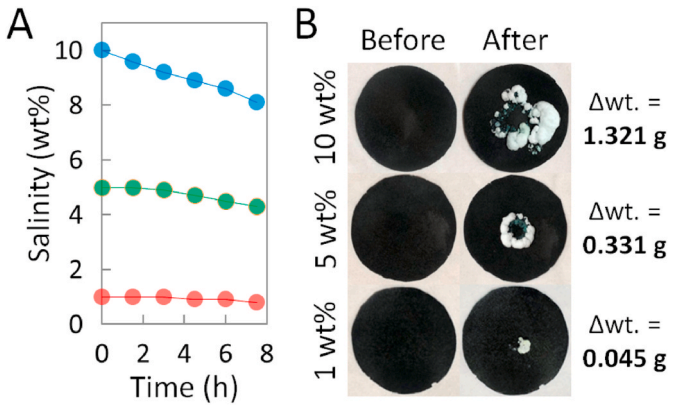

Fig. 7. (A) Salinity change over time for the bulk solutions with the initial NaCl concentrations equal to 10 wt% (blue curve), 5 wt% (green curve) and 1 wt% (red curve). Here the 195-μm pore size, water-repellent GeNPs-coated oxidized CF in 6 cm diameter disk with the underlying cellulose paper size equal to 2 cm × 2 cm was used. The one sun solar irradiation lasted for 7.5 h and the salinity of the bulk solution was measured every 0.5 h. (B) Photographs of the CFs before and after the salt extraction process. With the initial NaCl concentrations equal to 10 wt%, 5 wt% and 1 wt%, the extracted dry salt masses are equal to 1.321 g, 0.331 g and 0.045 g, respectively. (For interpretation of the references to color in this figure legend, the reader is referred to the Web version of this article).

stability study.

By taking advantage of the irreversible process of dry salt formation as discussed above, we demonstrate salt extraction (Fig. 7), by using the setup as shown in Fig. 1B. Instead of escaping into the environment, here the steam is confined within an enclosed system by covering the container with a glass slide which is slightly tilted by about 10° for facilitating the water condensate to go back to the bulk solution. As the solar irradiation continues, more dry salts accumulate and remain on the CF surface, and since the total water mass is kept constant, the salinity of the bulk solution gradually decreases. Experimentally, using the 195-μm pore size, water-repellent GeNPs-coated oxidized CF in 6 cm diameter disk with the underlying cellulose paper size equal to 2 cm × 2 cm, the salinities of the bulk NaCl solutions (70 g) drop from the initial 10 wt%, 5 wt% and 1 wt% to 8.1 wt%, 4.3 wt% and 0.8 wt%, respectively, in 7.5 h under continuous one sun solar irradiance (Fig. 7A). Furthermore, the salinity decrease over time can be well fitted with an exponential function obtained from the theoretical analysis (SI Fig. S14). By comparing the CF weights before and after the salt extraction process, dry salt masses of 1.321, 0.331 and 0.045 g for the initial NaCl concentrations equal to 10 wt%, 5 wt% and 1 wt% were obtained (Fig. 7B). The dry salt masses divided by the total solution mass (70 g), which is maintained constant during the evaporation process, are nearly the same as the decreased salinities in Fig. 7A. The slight difference should result from the wet salts staying on the cellulose paper which are not counted into the dry salt mass.

3. Conclusion

In summary, we demonstrate solar steam generation with high evaporation rates and extraction of dry salts from solutions by using the water-repellent GeNPs-coated oxidized CFs as light absorbers and heat concentrators. The CF surface was first oxidized into black CuO, then dip-coated with colloidal GeNPs for enhancing infrared absorption, and lastly treated with TCPFOS to render hydrophobicity. The polycrystalline GeNPs, synthesized by a high energy ball milling method, have irregular flaky shapes with the majority particle size ranging from about 100 nm to 400 nm. The water-repellent GeNPs-coated oxidized CF can absorb more than 95% of the AM1.5G solar irradiance spectrum, for heating up a water-permeated cellulose paper underneath to generate steam, which is then evacuated through the CF's interconnected pores. Furthermore, due to the CF's high thermal conductivity (65.3 W m^{-1} K^{-1} for the 51-μm pore size CF), the heat generated in the CF's peripheral region can be efficiently concentrated to the center where the water evaporates. With the light-absorbing CF area about 7 times larger than the water-evaporating cellulose paper and the convective heat loss mitigated by a PMMA cover, under one sun solar irradiance, the central temperature of the 51-μm pore size CF can reach 74.3 °C, resulting in a high evaporation rate of 3.2 kg m^{-2} h^{-1} and a conversion efficiency of 29.1%. When a NaCl solution is used for evaporation inside an enclosed system in which the water condensate is recycled, since the water evaporation rate is greatly enhanced by the heat concentration, the wet salts accumulating on the cellulose paper cannot diffuse back to the bulk solution in time. As a result, the dry salts start to grow and remain on the hydrophobic CF surface. As the solar irradiation continues, more and more readily useful dry salts can be harvested, while the bulk solution is gradually desalinized. Experimentally, using a 6-cm-diameter 195-μm pore size CF with the underlying cellulose paper size equal to 2 cm × 2 cm, for a 70 g NaCl solution, 1.321 g of dry salts were obtained and the solution salinity decreased from the initial 10 wt% to 8.1 wt% in 7.5 h under one sun solar irradiance. The salinity decrease over time can be well fitted with an exponential function obtained from the theoretical analysis. The salt extraction method based on the heat-concentrating water-repellent GeNPs-coated oxidized CFs can be a green alternative to the conventional electrodialysis method.

CRediT authorship contribution statement

Yisu Xu: Conceptualization, materials preparation, measurements, and, writing. **Zhifu Qi:** Conceptualization. **Zhouyang Luo:** Conceptualization. **Zhen Shen:** Conceptualization. **Chenxi Li:** Conceptualization. **Guo Chen:** Materials preparation. **Wenyi Cai:** Materials preparation. **Hua Bao:** Advising. **Chang-Ching Tu:** Conceptualization, Supervision, revision and submission.

Declaration of competing interest

The authors declare that they have no known competing financial interests or personal relationships that could have appeared to influence the work reported in this paper.

Acknowledgement

This research was financially supported by the Zhejiang Energy Group R&D Institute Co., Ltd. (ZNKJ-2019-046).

Appendix A. Supplementary data

Supplementary data to this article can be found online at https://doi.org/10.1016/j.solmat.2021.111191.

References

[1] C.J. Vörösmarty, P. Green, J. Salisbury, R.B. Lammers, Global water resources: vulnerability from climate change and population growth, Science 289 (2000) 284–288.
[2] M. Elimelech, W.A. Phillip, The future of seawater desalination: energy, technology, and the environment, Science 333 (2011) 712–717.
[3] L. Malaeb, G.M. Ayoub, Reverse osmosis technology for water treatment: state of the art review, Desalination 267 (2011) 1–8.
[4] N.S. Lewis, Research opportunities to advance solar energy utilization, Science 351 (2016) aad1920.
[5] G.N. Tiwari, L. Sahota, Review on the energy and economic efficiencies of passive and active solar distillation systems, Desalination 401 (2017) 151–179.
[6] P. Tao, G. Ni, C. Song, W. Shang, J. Wu, J. Zhu, G. Chen, T. Deng, Solar-driven interfacial evaporation, Nat. Energy 3 (2018) 1031–1041.
[7] Y. Pang, J. Zhang, R. Ma, Z. Qu, E. Lee, T. Luo, Solar–thermal water evaporation: a review, ACS Energy Lett 5 (2020) 437–456.
[8] C. Chen, Y. Kuang, L. Hu, Challenges and opportunities for solar evaporation, Joule 3 (2019) 683–718.

[9] Y. Liu, S. Yu, R. Feng, A. Bernard, Y. Liu, Y. Zhang, H. Duan, W. Shang, P. Tao, C. Song, T. A Bioinspired Deng, Reusable, Paper-based system for high-performance large-scale evaporation, Adv. Mater. 27 (2015) 2768–2774.
[10] L. Zhou, Y. Tan, D. Ji, B. Zhu, P. Zhang, J. Xu, Q. Gan, Z. Yu, J. Zhu, Self-assembly of highly efficient, broadband plasmonic absorbers for solar steam generation, Sci. Adv. 2 (2016), e1501227.
[11] J. Fang, Q. Liu, W. Zhang, J. Gu, Y. Su, H. Su, C. Guo, D. Zhang, Ag/Diatomite for highly efficient solar vapor generation under one-sun irradiation, J. Mater. Chem. 5 (2017) 17817–17821.
[12] L. Zhou, Y. Tan, J. Wang, W. Xu, Y. Yuan, W. Cai, S. Zhu, J. Zhu, 3D self-assembly of aluminum nanoparticles for plasmon-enhanced solar desalination, Nat. Photonics 10 (2016) 393–398.
[13] Z. Liu, H. Song, D. Ji, C. Li, A. Cheney, Y. Liu, N. Zhang, X. Zeng, B. Chen, J. Gao, Y. Li, X. Liu, D. Aga, S. Jiang, Z. Yu, Q. Gan, Extremely cost-effective and efficient solar vapor generation under nonconcentrated illumination using thermally isolated black paper, Global Challenges 1 (2017) 1600003.
[14] H. Ghasemi, G. Ni, A.M. Marconnet, J. Loomis, S. Yerci, N. Miljkovic, G. Chen, Solar steam generation by heat localization, Nat. Commun. 5 (2014) 4449.
[15] J. Yang, Y. Pang, W. Huang, S.K. Shaw, J. Schiffbauer, M.A. Pillers, X. Mu, S. Luo, T. Zhang, Y. Huang, G. Li, S. Ptasinska, M. Lieberman, T. Luo, Functionalized graphene enables highly efficient solar thermal steam generation, ACS Nano 11 (2017) 5510–5518.
[16] N. Xu, X. Hu, W. Xu, X. Li, L. Zhou, S. Zhu, J. Zhu, Mushrooms as efficient solar steam-generation devices, Adv. Mater. 29 (2017) 1606762.
[17] Y. Li, T. Gao, Z. Yang, C. Chen, W. Luo, J. Song, E. Hitz, C. Jia, Y. Zhou, B. Liu, B. Yang, L. Hu, 3D-Printed, all-in-one evaporator for high-efficiency solar steam generation under 1 sun illumination, Adv. Mater. 29 (2017) 1700981.
[18] J. He, Z. Zhang, C. Xiao, F. Liu, H. Sun, Z. Zhu, W. Liang, A. Li, High-performance salt-rejecting and cost-effective superhydrophilic porous monolithic polymer foam for solar steam generation, ACS Appl. Mater. Interfaces 12 (2020) 16308–16318.
[19] J. He, Y. Fan, C. Xiao, F. Liu, H. Sun, Z. Zhu, W. Liang, A. Li, Enhanced solar steam generation of hydrogel composite with aligned channel and shape memory behavior, Compos. Sci. Technol. 204 (2021) 108633.
[20] F. Wang, Z. Hu, Y. Fan, W. Bai, S. Wu, H. Sun, Z. Zhu, W. Liang, A. Li, Salt-rejection solar absorbers based on porous ionic polymers nanowires for desalination, Macromol. Rapid Commun. 42 (2021) 2000536.
[21] N. Li, D. Yin, L. Xu, H. Zhao, Z. Liu, Y. Du, High-quality ultralong copper sulphide nanowires for promising applications in high efficiency solar water evaporation, Mater. Chem. Front. 3 (2019) 394–398.
[22] J. Wang, Y. Li, L. Deng, N. Wei, Y. Weng, S. Dong, D. Qi, J. Qiu, X. Chen, T. Wu, High-performance photothermal conversion of narrow-bandgap Ti_2O_3 nanoparticles, Adv. Mater. 29 (2017) 1603730.
[23] G. Zhu, J. Xu, W. Zhao, F. Huang, Constructing black titania with unique nanocage structure for solar desalination, ACS Appl. Mater. Interfaces 8 (2016) 31716–31721.
[24] D. Ding, W. Huang, C. Song, M. Yan, C. Guo, S. Liu, Non-stoichiometric MoO_{3-x} quantum dots as a light-harvesting material for interfacial water evaporation, Chem. Commun. 53 (2017) 6744–6747.
[25] R. Chen, Z. Wu, T. Zhang, T. Yu, M. Ye, Magnetically recyclable self-assembled thin films for highly efficient water evaporation by interfacial solar heating, RSC Adv. 7 (2017) 19849–19855.
[26] L. Wang, Z. Yuan, Y. Zhao, Z. Guo, Review on development of small point-focusing solar concentrators, J. Therm. Sci. 28 (2019) 929–947.
[27] D. Barlev, R. Vidu, P. Stroeve, Innovation in concentrated solar power, Sol. Energy Mater. Sol. Cells 95 (2011) 2703–2725.
[28] K. Shanks, S. Senthilarasu, T.K. Mallick, Optics for concentrating photovoltaics: trends, limits and opportunities for materials and design, Renew. Sustain. Energy Rev. 60 (2016) 394–407.
[29] G. Ni, G. Li, S.V. Boriskina, H. Li, W. Yang, T. Zhang, G. Chen, Steam generation under one sun enabled by a floating structure with thermal concentration, Nat. Energy 1 (2016) 1–7.
[30] N. Heck, K.L. Petersen, D.C. Potts, B. Haddad, A. Paytan, Predictors of coastal stakeholders' knowledge about seawater desalination impacts on marine ecosystems, Sci. Total Environ. 639 (2018) 785–792.
[31] M. Reig, S. Casas, C. Aladjem, C. Valderrama, O. Gibert, F. Valero, C.M. Centeno, E. Larrotcha, J.L. Cortina, Concentration of NaCl from seawater reverse osmosis brines for the chlor-alkali industry by electrodialysis, Desalination 342 (2014) 107–117.
[32] Z. Ye, P.K. Srivastava, Y. Xu, W. Wang, L. Jing, S.-L. Chen, C.-C. Tu, Surface-functionalized silicon nanoparticles as contrast agents for photoacoustic microscopy imaging, ACS Appl. Nano Mater. 2 (2019) 7577–7584.
[33] S. Han, G. Chen, C. Shou, H. Peng, S. Jin, C.-C. Tu, Visibly transparent solar windows based on colloidal silicon quantum dots and front-facing silicon photovoltaic cells, ACS Appl. Mater. Interfaces 12 (2020) 43771–43777.
[34] X. Liu, M. Atwater, J. Wang, Q. Huo, Extinction coefficient of gold nanoparticles with different sizes and different capping ligands, Colloids Surf., B 58 (2007) 3–7.
[35] P. Broqvist, A. Alkauskas, A. Pasquarello, Defect levels of dangling bonds in silicon and germanium through hybrid functionals, Phys. Rev. B 78 (2008), 075203.
[36] N. Xu, J. Li, Y. Wang, C. Fang, X. Li, Y. Wang, L. Zhou, B. Zhu, Z. Wu, S. Zhu, J. Zhu, A water lily-inspired hierarchical design for stable and efficient solar evaporation of high-salinity brine, Sci. Adv. 5 (2019), eaaw7013.
[37] M. Zhu, Y. Li, F. Chen, X. Zhu, J. Dai, Y. Li, Z. Yang, X. Yan, J. Song, Y. Wang, E. Hitz, W. Luo, M. Lu, B. Yang, L. Hu, Plasmonic wood for high-efficiency solar steam generation, Adv. Energy Mater. 8 (2018) 1701028.
[38] G. Ni, S.H. Zandavi, S.M. Javid, S.V. Boriskina, T.A. Cooper, G. Chen, A salt-rejecting floating solar still for low-cost desalination, Energy Environ. Sci. 11 (2018) 1510–1519.